

Ultrafast Terahertz Conductivity Dynamics in Mesoporous TiO₂: Influence of Dye Sensitization and Surface Treatment in Solid-State Dye-Sensitized Solar Cells

Priti Tiwana, Patrick Parkinson, Michael B. Johnston, Henry J. Snaith,* and Laura M. Herz*

University of Oxford, Department of Physics, Clarendon Laboratory, Parks Road, Oxford, OX1 3PU, United Kingdom

Received: September 10, 2009; Revised Manuscript Received: November 25, 2009

We have used optical-pump terahertz-probe spectroscopy to explore the photoinduced conductivity dynamics in mesoporous anatase TiO₂ films, commonly employed as the electron-transporting electrode in dye-sensitized solar cells. We find an intrinsic mobility value of 0.1 cm²/(V s) and diffusion length of ~20 nm for electron motion through the TiO₂ matrix. The photoconductivity dynamics in TiO₂ films, both before and after sensitization with a ruthenium bipyridyl complex termed Z907, were examined in order to study the charge injection, trapping, and recombination time scales. We observe a biphasic charge injection from Z907, with a fast sub-500 fs component, followed by a slower 70–200 ps component. This is followed by photoconductivity decay over the first few nanoseconds, predominantly reflecting charge carrier trapping. In addition, we have utilized terahertz spectroscopy to investigate the influence of treating the titania surface with TiCl₄ on early-time charge dynamics. In the solar cells, surface treatment of the mesoporous TiO₂ with TiCl₄ is critical to enable efficient operation. Here, we find that neither early-time charge mobility nor charge injection rate or decay times are significantly affected by the treatment, which suggests that it may, instead, have an impact on phenomena occurring on longer time scales.

Introduction

Dye-sensitized solar cells (DSCs) offer a promising solution to the urgent need for a cheap source of renewable energy.^{1,2} A typical DSC is designed as an electrochemical cell consisting of a mesoporous network of an electron-transporting material, usually interconnected TiO₂ nanoparticles, sensitized with light-absorbing dye molecules and infiltrated with a redox-active electrolyte or solid-state hole transporter.³ This film is contacted on both sides with electrodes to complete the device. Light absorption in the dye results in rapid electron injection from the dye excited state into the TiO₂ conduction band.⁴ These electrons are then transported through the TiO₂ matrix via diffusion and are finally collected at the transparent conducting anode. Meanwhile, the oxidized dye molecules are regenerated by electrons donated from the electrolyte or hole transporter, and the positive charge is transported to the cathode, completing the circuit.^{5,6} To date, efficiencies of 11.2% and 5.1% have been achieved using a redox-active liquid electrolyte and a solid organic hole transporter (spiro-OMeTAD) as the hole transporter, respectively.^{7,8} However, these values are still much lower than the 25% efficiency achieved using first-generation single-crystal silicon solar cells,⁹ and significant effort is being invested to reduce this gap, in order to improve the commercial viability of DSCs.

The electron transport mechanism in the TiO₂ mesoporous network is a critical step that affects overall device performance. Over the past few decades, a large amount of theoretical and experimental work has been carried out to allow a better understanding of electron injection into and movement through the semiconductor matrix toward the electrode, with the aim of increasing the charge generation and collection efficiency.^{10–22} However, most of the current understanding of the electron

dynamics in TiO₂ is based on indirect estimates derived from the application of electron-transport models. These include various modifications of the Drude model,^{13,23} effective medium theory,¹⁵ or Monte Carlo^{24,25} or FTDT simulations.²⁶ Time-resolved microwave conductivity (TRMC) measurements offer a useful photoconductivity probe but can only achieve nanosecond temporal resolution.¹⁶ In the present study, we have used optical-pump terahertz-probe (OPTP) spectroscopy to measure the change in photoconductivity in TiO₂ as a function of probe delay with respect to an excitation pulse, in the subpicosecond to nanosecond time range.

Being an all-optical technique, OPTP is an excellent probe for measuring charge dynamics in nanostructured materials,^{27,28} avoiding any artifacts arising from electronic contact to the mesoporous semiconductor film. Additionally, unlike most photocurrent measurement techniques, OPTP experiments can be conducted on bare TiO₂, without the need to fill the film with an electrolyte in order to complete the circuit. Thus, this technique allows us to probe the intrinsic (or local) properties of the semiconductor. Here, we have measured the transient photoinduced conductivity in the subnanosecond time range, for mesoporous TiO₂ films with and without dye sensitization. These measurements enable direct assessment of the charge injection rate, mobility, recombination, and trapping on this time scale. The effect of treating TiO₂ films with TiCl₄ on charge injection and trapping rates has also been probed, with the intention of identifying the mechanisms that result in increased photocurrent and efficiency in TiCl₄-treated DSCs. Information obtained from studying photoconductivity dynamics can be crucial in answering questions about the efficacy of different dye sensitizers and of various surface treatments in improving charge injection and electron diffusion lengths in the DSCs and, therefore, provides valuable input for the optimization of electron transport and device performance.

* To whom correspondence should be addressed. E-mail: h.snaith@physics.ox.ac.uk (H.J.S.), l.herz@physics.ox.ac.uk (L.M.H.).

Experimental Section

Samples for Terahertz Study. Z-cut quartz was chosen as a substrate because of its transparency in the optical and terahertz (THz) frequency range. After cleaning the substrates with acetone and IPA, an ~ 100 nm thick compact layer of TiO_2 was deposited at 450°C using aerosol spray pyrolysis.²⁹ A home-made TiO_2 paste made with ~ 20 nm anatase TiO_2 nanoparticles using a method similar to that presented by Barbe et al.³⁰ was spin-coated on the substrates, and the samples were then slowly sintered in air at 500°C . This process yielded $2\text{--}4\ \mu\text{m}$ thick transparent TiO_2 films (thickness measured with a Veeco DekTak 150 surface profiler) with $\sim 60\%$ porosity.³ To understand the effect of TiCl_4 treatment on TiO_2 -based DSCs, some of the TiO_2 films were soaked in a 20 mM aqueous solution of TiCl_4 for 4 h at room temperature in the dark. After rinsing with DI water and drying in air, the films were then resintered to 500°C for 45 min.

The mesoporous TiO_2 samples were sensitized by soaking the samples in dye solution overnight in the dark at room temperature. The dye solution comprised 0.3 mM Z907 in acetonitrile/*tert*-butanol (1:1 vol %) solvent. Z907 is an amphiphilic polypyridyl ruthenium complex, $\text{NaRu}(4\text{-carboxylic acid-4'-carboxylate})(4,4'\text{-dinonyl-2,2'-bipyridine})(\text{NCS})_2$, with two of the carboxylate groups in the N3 dye replaced by hydrophobic nonyl chains.⁴ The alkyl chains are intended to help form a more compact monolayer of the dye on the TiO_2 surface and also act as a blocking layer between the hole conductor and TiO_2 , thus resulting in faster charge injection and reduced recombination.^{31,32}

DSC Devices. Complete solid-state DSCs were fabricated using the method outlined in ref 29. TiO_2 paste purchased from Dyesol (18NR-T) was doctor-bladed on fluorine-doped tin oxide (FTO) glass sheets and then slowly sintered at 500°C in air, resulting in $1.4\ \mu\text{m}$ thick films. Similar to the case of the samples for THz measurements, some of these films were soaked in 20 mM aqueous TiCl_4 for 4 h at room temperature in the dark. After resintering at 500°C , the samples were then dye-sensitized with Z907. Spiro-OMeTAD (2,2',7,7'-tetrakis(*N,N*-dimethoxyphenyl-amine)-9,9'-spirobifluorene) dissolved in chlorobenzene was used as the hole-transporting material (HTM), with *tert*-butyl pyridine (*t*BP) and bis(trifluoromethyl-sulfonyl)amine lithium salt (Li-TFSI) (dissolved separately in acetonitrile) used as additives for improved device performance.²⁹ Finally, 150 nm thick silver electrodes were evaporated over the HTM layer under high vacuum (10^{-6} mbar) to complete the devices.

Optical Pump Terahertz Probe (OPTP) Spectroscopy. Photoconductivity transients were measured using an OPTP setup similar to that described in ref 27. Briefly, 800 nm wavelength pulses of ~ 40 fs duration originating from a Spectra-Physics Spitfire amplifier are used to generate either 400 nm pulses through frequency-doubling with a BBO crystal or 475–700 nm pulses by pumping an optical parametric amplifier (TOPAS, Spectra-Physics). Photoexciting the sample with these pulses results in electrons being promoted into the TiO_2 conduction band, where they are mobile and can interact with the THz probe pulse, incident on the sample at a time τ after the excitation pulse. The change in amplitude and phase of the THz probe pulse transmitted through the photoexcited sample is measured using a double lock-in technique²³ and gives a direct measure of the photoconductivity of the sample material in the 0.2–2.0 THz frequency range. In this study, we measure the change in amplitude of the peak value of the THz pulse, $\Delta T/T$ and use eq 1 to calculate the variation in photoconductivity of the sample $\Delta\sigma$ as a function of the probe delay, τ .³³

$$\Delta\sigma(\tau) = -\frac{\epsilon_0 c(n_a + n_b) \Delta T(\tau)}{L T(\tau)} \quad (1)$$

Here, ϵ_0 is the free-space permittivity, c is the speed of light, and L is the optical penetration depth or the sample thickness, whichever is smaller. n_a and n_b are the refractive indices of the media immediately before and after the photoexcited material, respectively, in the THz frequency range. n_b is, therefore, the refractive index of either the substrate (quartz, 1.95) or of nonphotoexcited TiO_2 (~ 2.5),¹³ depending on the absorption depth (which is a function of wavelength). It is important to note that, because the optical penetration depth is comparable to sample thickness in our case, the true conductivity is a function of the depth z inside the sample, whereas the conductivity evaluated in eq 1 is the average value:

$$\sigma(\tau) = \int_0^L \sigma(\tau, z) dz \quad (2)$$

Temporal overlap of the pump and probe pulses can lead to analytical complications in accounting for the changing photoexcited sample properties while it is being probed by the picosecond-duration THz pulse.^{33,34} We have, therefore, not presented an in-depth analysis of the charge injection dynamics, and our simplified scheme is valid only for $\tau \gtrsim 3$ ps. All pump–probe experiments in this study were performed at room temperature and under vacuum ($<10^{-3}$ mbar pressure). The incident pump fluence was kept low in order to avoid charge–charge interactions,³⁵ typically at about $10^{13}\text{--}10^{14}$ photons/cm²/pulse. This is equivalent to the solar energy incident on a DSC under standard operating conditions. Sample integrity was checked before and after the experiments by measuring the steady-state absorption spectrum to verify negligible sample degradation.

Current–Voltage Measurements. Photovoltaic performance of the DSCs was measured by scanning the current–voltage characteristics in the dark and under simulated sunlight calibrated to give the equivalent of AM 1.5 illumination at 100 mW/cm². The calibration was performed using a calibrated Si reference cell with a KG5 filter to minimize spectral mismatch.

Results and Discussion

Carrier Mobility in Bare TiO_2 . We first probe the photoconductivity dynamics in bare TiO_2 samples (without dye sensitization). Figure 1a,b shows the early- and later-time variation in photoconductivity as a function of probe delay, τ , for an as-sintered TiO_2 sample excited at either 400 or 550 nm with an $\sim 3 \times 10^{14}$ photons/cm² incident fluence, measured under low vacuum. We also show the UV–vis absorption spectra for mesoporous TiO_2 films with and without dye and with and without TiCl_4 treatment in Figure 1c. For photoexcitation at 400 nm, close to the anatase TiO_2 band gap,^{22,36} we observe a resolution-limited rise time $t_{1/2}$ of ~ 500 fs in the photoconductivity. It has already been demonstrated that the photoconductivity in TiO_2 is dominated by the electron response.^{14,17} This ultrafast rise, therefore, indicates direct excitation of electrons into the conduction band (CB) or into sites lying close to the CB, which may form a mobility edge. On the longer time scale, a slower decay in photoconductivity is observed with a lifetime of ~ 1.5 ns. The photoconductivity, $\sigma(\tau)$, is a function of both the carrier mobility $\mu(\tau)$ and the number of mobile carriers $N(\tau)$ that can interact with the THz pulse, as $\sigma(\tau) = N(\tau)e\mu(\tau)$, where e is the electronic charge. Thus, the observed decay in conductivity illustrates either reduced mobility as τ increases or decreased number of mobile

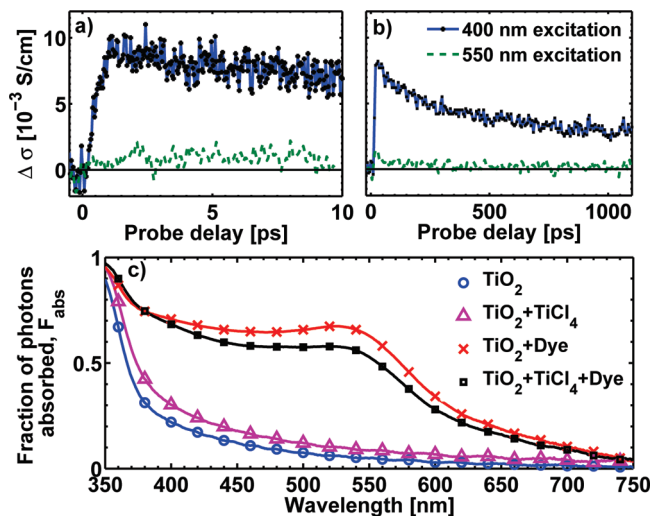


Figure 1. (a) Early-time and (b) later-time photoconductivity dynamics in mesoporous TiO₂ upon photoexcitation at 400 nm (blue solid line with black crosses) and 550 nm (green dashed line), with an incident fluence of $\sim 3 \times 10^{14}$ photons/cm² and pulse duration of ~ 40 fs. A photoconductivity rise “half-time” of ~ 500 fs is observed, followed by a slow decay over 1–2 ns. (c) Steady-state absorption spectra of TiO₂ samples with and without TiCl₄ treatment, both before and after dye sensitization.

electrons due to charge trapping and/or recombination, or a combination of all three factors.

Monte Carlo simulations in combination with transient photocurrent and transient absorption spectroscopy measurements have revealed that the electron transport through the TiO₂ network predominantly occurs in the conduction band, with the conduction band electrons being populated by multiple trapping–detrapping events from the energetically distributed intra-band-gap states.^{10,11} This multitrapping mode of charge transport will result in decreasing average charge mobility $\mu(\tau)$ with increasing time τ after photoexcitation. As τ increases, mobile electrons will become immobilized in sub-band-gap traps in TiO₂, while some electrons will be lost through recombination within the TiO₂ film. Our experimental observation of photoconductivity decay over the first couple of nanoseconds corroborates this discussion and suggests that this is a typical trapping time scale.

For practical analysis, extraction of the carrier mobility value is more useful than the photoconductivity because the mobility is independent of both sample geometry and excitation fluence. We, therefore, define an “effective mobility”, $\phi_{\text{inj}}\mu_{\text{peak}}$, as the product between the peak charge mobility value μ_{peak} at delay time $\tau = \tau_{\text{peak}}$ (when the highest photoconductivity signal $\Delta\sigma_{\text{peak}}$ is measured) and the quantum yield ϕ_{inj} for charge separation per absorbed photon (or electron injection efficiency in the case of a dye-sensitized sample). $\phi_{\text{inj}}\mu_{\text{peak}}$ is calculated from experimental observables through

$$\phi_{\text{inj}}\mu_{\text{peak}} = \frac{\Delta\sigma_{\text{peak}}}{eF_{\text{abs}}N_{\text{incident}}} \quad (3)$$

where N_{incident} is the incident photon density. F_{abs} is the fraction of photons absorbed in the photoexcited region of the sample, derived from the steady-state absorption spectrum of the sample taken with a Cary 300 spectrophotometer equipped with a “Labsphere” integrating sphere (see Figure 1c).

Figure 2 shows values of $\phi_{\text{inj}}\mu_{\text{peak}}$ extracted in this manner for different films as a function of excitation fluence. For as-sintered TiO₂ obtained from EPFL (black Δ 's), an average value

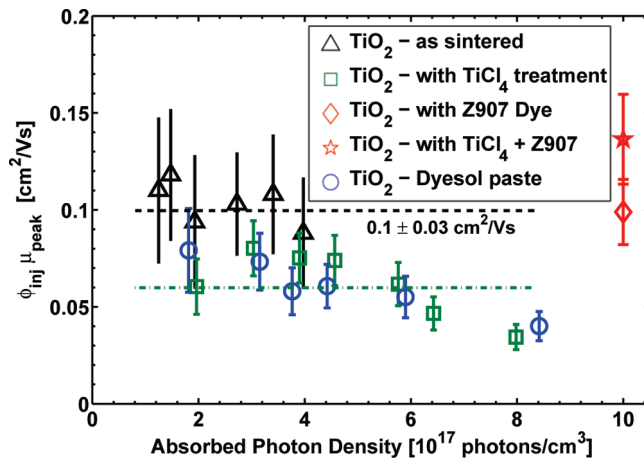


Figure 2. Fluence dependence of the effective carrier mobility in TiO₂ upon photoexcitation at 400 nm. The absorbed photon density was calculated from the incident fluence and the UV–vis absorption at 400 nm. All but one of the data sets were measured on samples prepared with homemade TiO₂ paste. The samples were as-sintered TiO₂ (black Δ), TiO₂ with TiCl₄ treatment (green \square), TiO₂ with Z907 dye (red \diamond), TiO₂ with TiCl₄ treatment and Z907 dye (red \star), and TiO₂ made with dyesol paste 18NR-T (blue \circ). Assuming near unity charge injection efficiency, the average carrier mobility is determined to be 0.1 ± 0.03 cm²/(V s) for TiO₂ samples made with homemade paste (black dashed line) and 0.06 ± 0.01 cm²/(V s) for TiO₂ films treated with TiCl₄ (green dashed-dotted line).

of 0.1 ± 0.03 cm²/(V s) is observed, whereas samples made using anatase TiO₂ paste purchased from Dyesol (18NR-T) (blue \circ 's) exhibit a similar value of 0.06 ± 0.01 cm²/(V s). We expect to obtain near unity charge generation efficiency from direct light absorption into TiO₂ near its band gap, thus suggesting that the $\phi_{\text{inj}}\mu_{\text{peak}}$ values derived here should be very close to the actual peak mobility values of the respective materials or, at least, should mark the lower limit on the mobility values.

In addition, Figure 2 shows that the carrier mobility is independent of the absorbed photon fluence for most of the range explored, with a small decrease at very high fluences that may, however, be due to experimental variation. In agreement, other researchers have noted that the incident fluence range over which our data were taken is low enough to avoid charge–charge interaction effects.^{13,15,16} This also suggests that the early-time conduction band mobility is being probed in the present study, rather than trap-limited mobility, which is understood to increase with increasing fluence owing to the gradual filling of the deep bulk trapping sites as the intensity (total number of electrons formed) increases.^{16,19}

The carrier mobility values extracted from our measurements can be compared with those previously determined by others for mesoporous TiO₂ films. Hendry et al. reported a mobility value of 0.01 cm²/(V s) measured using a THz pump–probe technique similar to the one used in our study.¹⁵ However, Hendry's study was based on a TiO₂ paste made using Degussa P25 nanoparticles that are a mixture of 80% anatase and 20% rutile TiO₂, unlike the 100% anatase TiO₂ paste used in this study (as determined by XRD). On the other hand, a much higher mobility value of 15 cm²/(V s) was reported by Turner et al. also for a mixture of anatase and rutile TiO₂ nanoparticles,¹³ using data analysis based on the Drude–Smith model.³⁷ In addition to the standard Drude model that describes a free electron gas undergoing random elastic scattering events, Turner et al. have introduced an extra factor attributed to 90% backscattering from the grain boundaries and nanoparticle surfaces. As a result, the modified Drude model yields higher

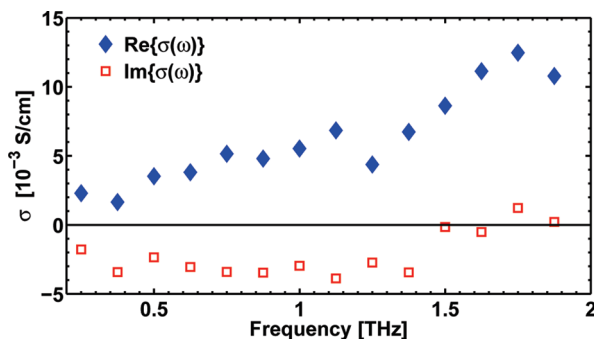


Figure 3. Real and imaginary parts of the TiO₂ conductivity spectrum in the 0.2–2.0 THz range. $\text{Re}\{\sigma(\omega)\}$ increases as the frequency increases from dc to 2 THz.

scattering time values as compared with estimates from other models, such as the effective medium theory.¹⁵ This results in the extracted mobility value being higher by a couple of orders of magnitude. In contrast, in our study presented here, the carrier mobility has been directly extracted from experimentally measurable parameters, without employing any data-fitting models, and is, hence, the most direct method for estimating the true ac mobility in mesoporous TiO₂.

Time-resolved microwave conductivity (TRMC) experiments at 9 GHz probe frequency have yielded carrier mobility values similar to the ones we find, ranging between 0.034 cm²/(V s) (using 9 nm anatase TiO₂ nanoparticles purchased from Solaronix¹⁶) and 0.5 cm²/(V s) (thin anatase TiO₂ film deposited using electron beam evaporation¹⁷). However, much lower mobility values of $\sim 1 \times 10^{-3}$ cm²/(V s) and $\sim 7 \times 10^{-6}$ cm²/(V s) have been reported with transient and quasi-steady-state photocurrent experiments^{20,21} and time-of-flight (TOF) measurements,²² respectively, carried out at room-temperature. This difference is not unexpected because the latter experimental techniques probe electron motion over a longer time scale (microsecond to second time range) corresponding to charge transport over longer distances for which initially mobile electrons have already experienced multiple trapping and detrapping events. The effect of probe-frequency dependence of the conductivity in mesoporous TiO₂ is also demonstrated in Figure 3, which shows that the real part of sample conductivity, and hence carrier mobility, increases as the probe frequency increases from dc (steady-state measurements) to terahertz domain. The spectrum was obtained by calculating the Fourier transform of the time-domain THz waveform transmitted through the sample, in accordance with previous THz studies on TiO₂.^{13,15} Transient THz time-domain spectroscopy thus provides crucial information regarding both the time and the frequency dependence of the photoinduced charge conductivity.

From the extracted mobility values, we may estimate the electron diffusion coefficient, D_e , using the Einstein equation

$$D_e = \frac{k_B T \mu}{e} \quad (4)$$

where k_B is the Boltzmann constant and T the temperature. We find a diffusion coefficient of approximately 2.5×10^{-3} cm²/s that we use to calculate the diffusion length through the relationship

$$l_e = \sqrt{D_e \tau_e} \quad (5)$$

We take the electron lifetime τ_e to be ~ 1.5 ns, as determined above from typical later-time THz conductivity decay scans shown in Figure 1b). From this, we determine a diffusion length,

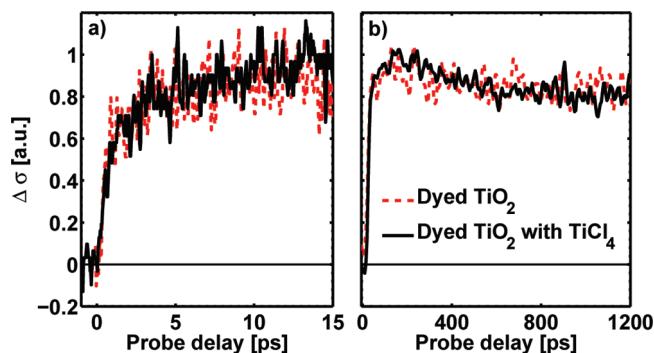


Figure 4. (a) Early-time (excitation at 625 nm) and (b) later-time dynamics (excitation at 500 nm) in dye-sensitized TiO₂ with (black solid line) and without (red dashed line) TiCl₄ treatment for an excitation fluence of $\sim 3 \times 10^{14}$ photons/cm². The curves have been normalized at their respective maxima. Similar trends are observed for excitation at wavelengths between 475 and 700 nm, although only selected data are shown here.

l_e , of 20 nm, which is surprisingly close to the nanoparticle diameter (~ 20 nm). We note however, that this value is much larger than the estimated electron mean free path of 1–2 nm in nanostructured TiO₂,^{13,14} promoting the question as to whether the motion of mobile electrons in the mesoporous matrix is limited more by the presence of sub-band-gap trap sites or by the physical geometrical constraints of the network. Because the traps are likely to predominantly reside near the nanoparticle surface, this is rather difficult to distinguish.

In their previous work, Hendry et al. reported the electron mobility and diffusion coefficient in bulk rutile TiO₂ to be ~ 1 cm²/(V s) and 0.025 cm²/s, respectively,^{14,15} and attributed the low values to the strong electron–phonon coupling in TiO₂. In addition to this factor, the values measured in our study for mesoporous TiO₂ are further reduced by an order of magnitude, suggesting restricted electron movement because of both geometrical constraints and increased trap sites in the nanostructured material.

Additionally, in the current study, we have probed the carrier dynamics in sintered TiO₂ nanoparticles in a low-pressure air matrix. The measured mobility value, therefore, reflects charge dynamics in the nanostructured composite material. Because carrier mobility is a function of the dielectric constant of the medium in which the TiO₂ nanoparticles are embedded, our THz pump–probe measurements are expected to yield somewhat different results when performed on TiO₂ infiltrated with the hole transporter in the complete photovoltaic device, and this work is currently underway.

Effect of Dye Sensitization. As a subsequent part of the investigation, we probed the effect of sensitizing the TiO₂ films with Z907 dye. We find that, compared with bare TiO₂ samples, sensitization leads to higher photoinduced conductivities when exciting at 400 nm. However, these increases can be entirely accounted for by the increased light absorption in the sample at 400 nm due to dye loading (see Figure 1c): calculating the effective mobility $\phi_{inj} \mu_{peak}$, as described above, we find very similar values to those for the undyed film, as shown in Figure 2 (compare Δ with \diamond).

Figure 4 shows the early-time photoconductivity transients following excitation of dye-sensitized TiO₂ at longer wavelengths (~ 475 to 700 nm) for which almost all charge injection into TiO₂ occurs via dye excited states, rather than through direct excitation of TiO₂. A biphasic charge injection process is observed, with the initial sub-500 fs rise time, followed by a slower 70–200 ps rise component. This is in stark contrast with

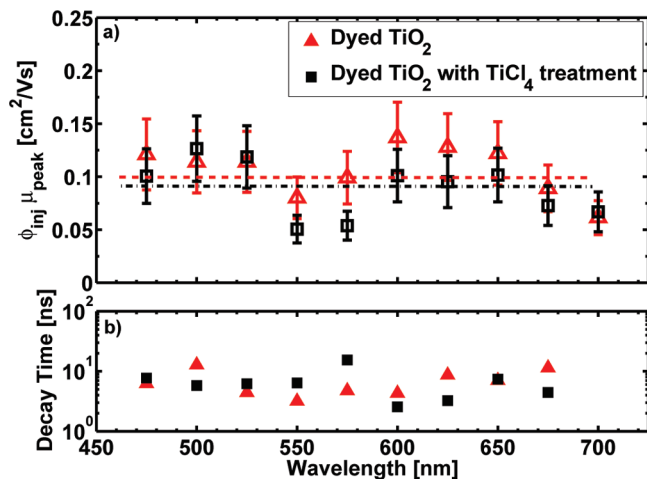


Figure 5. Variation in (a) effective mobility and (b) decay time as a function of excitation wavelength. Red triangles represent dye-sensitized TiO₂ and black squares represent dye-sensitized TiO₂ treated with TiCl₄. The absorbed fluence was about 10¹⁴ photons/cm². The dotted lines in (a) indicate the average mobility value for dye-sensitized TiO₂ with (0.09 cm²/(V s)) and without (0.1 cm²/(V s)) TiCl₄ treatment.

the single-phase ultrafast injection observed in undyed TiO₂ upon photoexcitation at 400 nm, as shown in Figure 1a. Similar biphasic charge injection kinetics have been observed by other groups, who have suggested that they are caused by injection from the singlet and triplet excited states of the ruthenium complex,^{38,39} injection from energetically or spatially diverse sites from the dye into TiO₂,⁴⁰ or because of aggregated or loosely attached dye molecules on the TiO₂ surface.⁴¹ We will explore the origins of this slow rise component for injection via Z907 dye in future work.

The nanosecond photoconductivity dynamics of dye-sensitized TiO₂ are shown in Figure 4b for excitation at 500 nm. The photoinduced conductivity decays over this time window, similar to the case of bare TiO₂, albeit over a slower time period of ~4 to 5 ns. Transient absorption studies, which probe the charge density, do not usually show such a rapid early-time decay, suggesting that the decay in THz conductivity observed here is predominantly due to trapping of mobile electrons, rather than recombination of electrons and holes.^{18,19} Recombination in dye-sensitized TiO₂ has been observed to extend well into the longer microsecond–millisecond time regime. On the other hand, faster decay observed in bare TiO₂ in Figure 1b could be attributed to recombination of the mobile electrons with the holes generated in TiO₂ during photoexcitation, in addition to electron trapping. This change in decay rate upon dye sensitization has been noted in the past.¹⁷ We observe very similar early- and later-time trends when the dye-sensitized sample is photoexcited with wavelengths ranging between 475 and 700 nm, although data for only two excitation wavelengths are presented in Figure 4. We fitted the later-time photoconductivity scans with monoexponential decays to estimate the decay times, shown in Figure 5b as a function of excitation wavelength. Constant values are observed, which suggests that the trapping times are independent of the excitation wavelength. This is consistent with photoelectron transfer taking place directly into the conduction band for all excitations above the optical band gap of TiO₂.

We also determined the effective mobility $\phi_{inj}\mu_{peak}$ as a function of excitation wavelength (Figure 5a). A constant value of ~0.1 cm²/(V s) was found for excitation across the entire absorption spectrum of the dye. Assuming that charge mobility is largely independent of excitation wavelength, the data shown

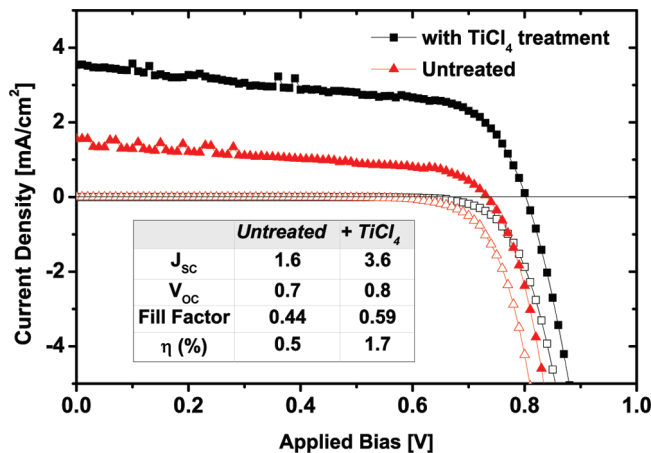


Figure 6. Current–voltage (*JV*) curves for solid-state DSCs fabricated with and without prior TiCl₄ treatment of the sintered TiO₂ electrodes, measured under simulated AM 1.5 solar illumination at an intensity of 100 mW/cm². The devices employ Z907 as the sensitizer dye and spiro-OMeTAD with Li-TFSI and *t*BP additives as the hole transporter.

in Figure 5a mainly reflect changes in the wavelength dependence of charge injection efficiency. Within experimental error and accounting for sample-to-sample variation, the injection efficiency appears to be independent of the excitation wavelength. The similarity between the $\phi_{inj}\mu_{peak}$ values for undyed and dyed TiO₂ further suggests that the charge generation efficiency for the two cases is similar. Because this dye has been used to fabricate high-efficiency devices, near unity injection efficiency is not unexpected.^{4,31}

Effect of TiCl₄ Treatment. Several research groups have previously reported consistently improved device performance when an extra layer of TiO₂ is grown on the surface of the sintered TiO₂ nanoparticles by treating the films with TiCl₄.^{30,42–45} However, the mechanisms underlying this improvement are still poorly understood. In this section, we investigate the impact of such TiCl₄ treatment on the early-time (subnanosecond) charge carrier injection and mobility in the TiO₂ mesoporous film.

To confirm the impact of TiCl₄ treatment on device performance, solid-state DSCs were fabricated with and without the surface treatment of the sintered TiO₂ film with TiCl₄, as described in the Experimental Section. As expected, the resulting photocurrent–voltage characteristics of the devices (shown in Figure 6) demonstrate a dramatic improvement in short-circuit current and efficiency with TiCl₄ treatment.

As discussed in detail by Sommeling et al.,⁴³ this improvement could be a result of increased light harvesting, higher charge injection efficiency, and/or increased collection efficiency, which, in turn, is a function of charge transport and recombination times. Increased particle necking between the TiO₂ nanoparticles caused by the TiCl₄ treatment has also been suggested as a reason for the improved charge transport.^{30,45} Transient photocurrent measurements, however, have revealed only a marginal improvement in charge transport.^{43,44} Decreased recombination and increased dye loading have also been observed by Sommeling et al., but they noted that the changes were not enough to explain the increased photocurrent. In agreement with their conclusion, we, in fact, obtain an enhancement in device performance with TiCl₄ treatment even though we consistently observe a decrease in dye absorption (see Figure 1c) because of the different preparation protocol we used. In their conclusion, Sommeling et al. have proposed that a positive shift in the TiO₂ conduction band could lead to increased charge

injection and that this may be the main reason for the enhanced device performance.

We have employed OPTP to probe the charge dynamics in TiO₂ films treated with TiCl₄, in order to investigate if the charge injection rate, carrier mobility, or trapping rate in the picosecond to nanosecond time range are affected as a consequence of the treatment. Figure 4 shows the resulting early- and later-time photoconductivity dynamics for dye-sensitized TiO₂ films with TiCl₄ treatment in comparison to as-sintered dyed TiO₂ films for a similar absorbed photon fluence. Contrary to expectation, we do not observe an increased charge injection rate as a result of the treatment, even when the samples are photoexcited at a range of wavelengths. We also find that TiCl₄ treatment appears to have little effect on the early-time carrier mobility. Figure 2 shows the effective mobility extracted from undyed TiO₂ films treated with TiCl₄ after excitation at 400 nm. Values of $\phi_{inj}t_{peak}$ of ~ 0.06 cm²/(V s) are observed, similar to those for samples without TiCl₄ treatment. In addition, the effective mobility was again determined for excitation of dyed samples across the absorption spectrum of the dye, as shown in Figure 5a, for both TiCl₄-treated and untreated films. We find no discernible differences between the two samples, suggesting that ϕ_{inj} is also largely unaffected by the TiCl₄ treatment. Finally, we have examined the effect of the treatment on the photoconductivity decay rate. Figure 4b shows identical decay dynamics for samples with and without TiCl₄ treatment, whereas Figure 5b demonstrates that the extracted decay times are identical for the two cases across the whole dye absorption spectrum. These observations demonstrate that the treatment does not affect carrier trapping at early times (up to a nanosecond), and thus, appears to have no significant effect on the density of sub-band-gap states in TiO₂. While these measurements are unable to yield the cause of the DSC performance enhancement with TiCl₄ treatment, they allow us to eliminate a number of possible scenarios. In particular, we clearly show that the TiCl₄ treatment has no effect on the pico- to nanosecond charge-injection, decay, and mobility dynamics in dye-sensitized TiO₂. These findings suggest that the origin of the increased photocurrents with TiCl₄ treatment may be found by investigating more closely the processes occurring on longer time scales (nanosecond to millisecond), such as hole transfer, charge separation, and longer time recombination processes. Finally, as a caveat to our findings, we note that careful spectroscopic analysis of complete devices under working conditions may yield information not attainable by studying dissected components, such as the dye-sensitized TiO₂ probed here.

Conclusions

We have investigated the photoconductivity dynamics in mesoporous TiO₂ films using an optical-pump terahertz-probe technique. We find an intrinsic electron mobility value of ~ 0.1 cm²/(V s) for both a homemade (EPFL) and a commercial (Dyesol) paste based on anatase TiO₂ nanoparticles. For TiO₂ films sensitized with Z907 dye, biphasic charge injection is observed, with an initial sub-500 fs fast component, followed by a slower 70–200 ps rise component. This is followed by a decay in photoconductivity over the first few nanoseconds, which appears to be caused by carrier trapping. In addition, we have probed the effect of TiCl₄ treatment of sintered TiO₂ in order to identify reasons for improved device performance seen in TiCl₄-treated DSCs. Repeated measurements on multiple samples show that the carrier mobility, charge injection efficiency, and charge trapping times are not affected by the treatment with TiCl₄ and are independent of the photoexcitation

wavelength. A thorough understanding of such charge generation and transport mechanisms can help us to identify the bottlenecks and, hence, to design better materials and material combinations for optimized photovoltaic device performance.

Acknowledgment. The authors thank Michael Grätzel and Pascal Comte from EPFL for supplying the homemade TiO₂ paste. This work was partly funded by EPSRC.

References and Notes

- Grätzel, M. *Prog. Photovoltaics* **2006**, *14*, 429–442.
- Grätzel, M. *Nature* **2001**, *414*, 338.
- Snaith, H. J.; Schmidt-Mende, L. *Adv. Mater.* **2007**, *19*, 3187–3200.
- Wang, P.; Wenger, B.; Humphry-baker, R.; Moser, J. E.; Teuscher, J.; Kantlehner, W.; Mezger, J.; Stoyanov, E. V.; Zakeeruddin, S. M.; Grätzel, M. *J. Am. Chem. Soc.* **2005**, *127*, 6850–6856.
- Oregan, B.; Grätzel, M. *Nature* **1991**, *353*, 737.
- Bach, U.; Lupo, D.; Comte, P.; Moser, J. E.; Weissortel, F.; Salbeck, J.; Spreitzer, H.; Grätzel, M. *Nature* **1998**, *395*, 583.
- Nazeeruddin, M. K.; Fantacci, S.; Selloni, A.; Viscardi, G.; Liska, P.; Ito, S.; Takeru, B.; Grätzel, M. *J. Am. Chem. Soc.* **2005**, *127*, 16835–16847.
- Snaith, H. J.; Moule, A. J.; Klein, C.; Meerholz, K.; Friend, R. H.; Grätzel, M. *Nano Lett.* **2007**, *7*, 3372.
- Green, M. A.; Emery, K.; Hishikawa, Y.; Warta, W. *Prog. Photovoltaics* **2009**, *17*, 85–94.
- Nelson, J.; Haque, S. A.; Klug, D. R.; Durrant, J. R. *Phys. Rev. B* **2001**, *6320*, 205321.
- van de Lagemaat, J.; Frank, A. J. *J. Phys. Chem. B* **2001**, *105*, 11194–11205.
- Tachibana, Y.; Rubtsov, I. V.; Montanari, I.; Yoshihara, K.; Klug, D. R.; Durrant, J. R. *J. Photochem. Photobiol., A* **2001**, *142*, 215–220.
- Turner, G. M.; Beard, M. C.; Schmittenmaer, C. A. *J. Phys. Chem. B* **2002**, *106*, 11716.
- Hendry, E.; Wang, F.; Shan, J.; Heinz, T. F.; Bonn, M. *Phys. Rev. B* **2004**, *69*, 081101.
- Hendry, E.; Koeberg, M.; O'Regan, B.; Bonn, M. *Nano Lett.* **2006**, *6*, 755.
- Kroeze, J. E.; Savenije, T. J.; Warman, J. M. *J. Am. Chem. Soc.* **2004**, *126*, 7608–7618.
- Kroeze, J. E.; Savenije, T. J.; Warman, J. M. *J. Photochem. Photobiol., A* **2002**, *148*, 49–55.
- Bach, U.; Tachibana, Y.; Moser, J. E.; Haque, S. A.; Durrant, J. R.; Grätzel, M.; Klug, D. R. *J. Am. Chem. Soc.* **1999**, *121*, 7445–7446.
- Tamaki, Y.; Furube, A.; Murai, M.; Hara, K.; Katoh, R.; Tachiya, M. *Phys. Chem. Chem. Phys.* **2007**, *9*, 1453.
- Petrozza, A.; Groves, C.; Snaith, H. J. *J. Am. Chem. Soc.* **2008**, *130*, 12912–12920.
- Kopidakis, N.; Schiff, E. A.; Park, N. G.; Frank, A. J. *J. Phys. Chem. B* **2000**, *104*, 3930–3936.
- Dittrich, T. *Phys. Status Solidi A* **2000**, *182*, 447.
- Beard, M. C.; Turner, G. M.; Schmittenmaer, C. A. *J. Phys. Chem. B* **2002**, *106*, 7146.
- Němec, H.; Kuěl, P. *Phys. Rev. B* **2009**, *79*, 115309.
- Nelson, J. *Phys. Rev. B* **1999**, *59*, 15374.
- Beard, M. C.; Schmittenmaer, C. A. *J. Chem. Phys.* **2001**, *114*, 2903–2909.
- Parkinson, P.; Lloyd-Hughes, J.; Gao, Q.; Tan, H. H.; Jagadish, C.; Johnston, M. B.; Herz, L. M. *Nano Lett.* **2007**, *7*, 2162–2165.
- Parkinson, P.; Joyce, H. J.; Gao, Q.; Tan, H. H.; Zhang, X.; Zou, J.; Jagadish, C.; Herz, L. M.; Johnston, M. B. *Nano Lett.* **2009**, *9*, 3349–3353.
- Snaith, H. J.; Schmidt-Mende, L.; Grätzel, M.; Chiesa, M. *Phys. Rev. B* **2006**, *74*, 045306.
- Barbe, C. J.; Arendse, F.; Comte, P.; Jirousek, M.; Lenzmann, F.; Shklover, V.; Grätzel, M. *J. Am. Ceram. Soc.* **1997**, *80*, 3157–3171.
- Schmidt-Mende, L.; Zakeeruddin, S. M.; Grätzel, M. *Appl. Phys. Lett.* **2005**, *86*, 013504.
- Snaith, H. J.; Zakeeruddin, S. M.; Schmidt-Mende, L.; Klein, C.; Grätzel, M. *Angew. Chem., Int. Ed.* **2005**, *44*, 6413.
- Nienhuys, H. K.; Sundström, V. *Phys. Rev. B* **2005**, *71*, 235110.
- Kuěl, P.; Kadlec, F.; Němec, H. *J. Chem. Phys.* **2007**, *127*, 11.
- Hendry, E.; Koeberg, M.; Pijpers, J.; Bonn, M. *Phys. Rev. B* **2007**, *75*, 233202.
- Tang, H.; Levy, F.; Berger, H.; Schmid, P. E. *Phys. Rev. B* **1995**, *52*, 7771–7774.
- Smith, N. V. *Phys. Rev. B* **2001**, *64*, 155106.
- Benko, G.; Kallioinen, J.; Korppi-Tommola, J. E. I.; Yartsev, A. P.; Sundström, V. *J. Am. Chem. Soc.* **2002**, *124*, 489–493.

- (39) Benko, G.; Kallioinen, J.; Myllyperkiö, P.; Trif, F.; Korppi-Tommola, J. E. I.; Yartsev, A. P.; Sundström, V. *J. Phys. Chem. B* **2004**, *108*, 2862–2867.
- (40) Tachibana, Y.; Nazeeruddin, M. K.; Grätzel, M.; Klug, D. R.; Durrant, J. R. *Chem. Phys.* **2002**, *285*, 127–132.
- (41) Wenger, B.; Grätzel, M.; Moser, J. E. *J. Am. Chem. Soc.* **2005**, *127*, 12150.
- (42) Nazeeruddin, M. K.; Kay, A.; Rodicio, I.; Humphrybaker, R.; Müller, E.; Liska, P.; Vlachopoulos, N.; Grätzel, M. *J. Am. Chem. Soc.* **1993**, *115*, 6382–6390.

- (43) Sommeling, P. M.; O'Regan, B. C.; Haswell, R. R.; Smit, H. J. P.; Bakker, N. J.; Smits, J. J. T.; Kroon, J. M. *J. Phys. Chem. B* **2006**, *110*, 19191.
- (44) O'Regan, B. C.; Durrant, J. R.; Sommeling, P. M.; Bakker, N. J. *J. Phys. Chem. C* **2007**, *111*, 14001.
- (45) Kambe, S.; Nakade, S.; Wada, Y.; Kitamura, T.; Yanagida, S. *J. Mater. Chem.* **2002**, *12*, 723.

JP908760R